

REPORT DOCUMENTATION PAGE

Form Approved
OMB No. 0704-0188

The public reporting burden for this collection of information is estimated to average 1 hour per response, including the time for reviewing instructions, searching existing data sources, gathering and maintaining the data needed, and completing and reviewing the collection of information. Send comments regarding this burden estimate or any other aspect of this collection of information, including suggestions for reducing the burden, to the Department of Defense, Executive Service Directorate (0704-0188). Respondents should be aware that notwithstanding any other provision of law, no person shall be subject to any penalty for failing to comply with a collection of information if it does not display a currently valid OMB control number.

PLEASE DO NOT RETURN YOUR FORM TO THE ABOVE ORGANIZATION.

1. REPORT DATE (DD-MM-YYYY) 01-07-2008		2. REPORT TYPE FINAL		3. DATES COVERED (From - To) 01-06-2005 to 31-05-2008	
4. TITLE AND SUBTITLE Aeromechanics of highly maneuverable bats				5a. CONTRACT NUMBER FA9550-05-1-0168	
				5b. GRANT NUMBER	
				5c. PROGRAM ELEMENT NUMBER	
6. AUTHOR(S) Swartz, S. M. Breuer, K. S.				5d. PROJECT NUMBER	
				5e. TASK NUMBER	
				5f. WORK UNIT NUMBER	
7. PERFORMING ORGANIZATION NAME(S) AND ADDRESS(ES) Brown University 164 Angell Street Providence, RI. 02912-9002				8. PERFORMING ORGANIZATION REPORT NUMBER	
9. SPONSORING/MONITORING AGENCY NAME(S) AND ADDRESS(ES)				10. SPONSOR/MONITOR'S ACRONYM(S)	
				11. SPONSOR/MONITOR'S REPORT NUMBER(S) AFRL-SR-AR-TR-08-0491	
12. DISTRIBUTION/AVAILABILITY STATEMENT Distribution A: Approved for Public Release					

20080820253

13. SUPPLEMENTARY NOTES

14. ABSTRACT
Bats fly with astounding agility, maneuverability and efficiency. Their flight mechanics are completely different from those of insects and birds and characterized by several unique aeromechanical features including: (i) complex three-dimensional articulated wing structures, (ii) flexible wing skeletons, (iii) anisotropic, highly elastic wing membrane skins and (iv) a network of shear stress sensors distributed over the wing surface. Over the three years of this project we have developed new tools and experimental systems for the study of bat flight. We have documented and quantified key aspects of bat flight behavior and of the mechanical properties of bat wing materials, and investigated key aspects of how the construction of the bat wing enables superior flight performance. Key findings include quantification of the complex but highly intercorrelated motions of the many joints of the bat wing, and delineation of possible wing joint motion combinations that can reproduce full 3D complexity with a simplified control scheme, and description of the complex wakes formed by bats during flight.

15. SUBJECT TERMS
flapping flight, bats, membrane wing

16. SECURITY CLASSIFICATION OF:			17. LIMITATION OF ABSTRACT	18. NUMBER OF PAGES	19a. NAME OF RESPONSIBLE PERSON
a. REPORT	b. ABSTRACT	c. THIS PAGE			19b. TELEPHONE NUMBER (Include area code)

Abstract:

Bats fly with astounding agility, maneuverability and efficiency. Their flight mechanics are completely different from those of insects and birds and characterized by several unique aeromechanical features including: (i) complex three-dimensional articulated wing structures, (ii) flexible wing skeletons, (iii) anisotropic, highly elastic wing membrane skins and (iv) a network of shear stress sensors distributed over the wing surface. Over the three years of this project we have developed new tools and experimental systems for the study of bat flight. We have documented and quantified key aspects of bat flight behavior and of the mechanical properties of bat wing materials, and investigated key aspects of how the construction of the bat wing enables superior flight performance. Key findings include quantification of the complex but highly intercorrelated motions of the many joints of the bat wing, and delineation of possible wing joint motion combinations that can reproduce full 3D complexity with a simplified control scheme, and description of the complex wakes formed by bats during flight.

Summary of Annual Accomplishments:

This project set out to quantify flight performance in living bats, the least studied of the living animal fliers. We have described the structural underpinnings of the bat wing, with special attention to the mechanical characteristics of the bones and wing membrane skin. We have developed novel videographic approaches to capture the complex three-dimensional kinematics of the wing during flight and to directly measure changes in the strain in the skin of the wing membrane. We have also developed PIV techniques well suited to studying the wakes of naturally flying bats, and implemented these techniques in two settings, flight corridors and wind tunnels. The flight corridor allows highly natural flight in which the bat can select its own flight speed and move through still air, presents a moderate technical challenge for PIV, and required a data analysis approach based on collation PIV samples from numerous flights. In the wind tunnel, investigators can control bat speed to a great degree, the technical issues for successful PIV are much more demanding, and high sampling rate allows time-resolved PIV of continuous flights.

EXPERIMENTAL EQUIPMENT, SET UP, AND PROCEDURES

Bats

We employed Lesser dog-faced fruit bats, *Cynopterus brachyotis*, for all live animal experiments supported by this program. We chose this species for analysis because they thrive in captivity, respond well to handling and training and, at a 35–45 g body mass and 30 to 40 cm wing span, are a good size for kinematic and PIV studies. Native to many forested areas of Southeast Asia, a colony of captive-bred individuals have been loaned to us by the Lubee Bat Conservancy (Gainesville, Florida). All bats are female, eliminating sex-specific variation. Reflective markers are attached to key anatomical landmarks using medical adhesive. The study subjects were trained both to fly in the flight corridor in both straight and turning configurations, and to fly in the low-speed wind tunnels at the Harvard University-Concord Field Station and in the Division of Engineering at Brown University.

Flight Corridor

All experiments were performed in an enclosed flight cage located at the Concord Field Station of Harvard University. The flight cage is 8 m long with a cross-sectional area of approximately 1 m (width) x 2 m (height). The x-axis is defined as the bat's flight direction, the y-axis is the transverse direction toward to the bat's left and the z-axis is the vertical direction. The origin of the coordinate system is defined as the point where the bat's sternum (approximately its center of mass) passes through the PIV laser sheet (discussed below). The bat flies through the flight cage, and her body and wing movements are captured by a pair of Redlake high-speed, low-light sensitive video cameras (MotionScope PCI 1000, operating at a frame rate of 500 images s⁻¹). Both cameras are positioned on the floor looking upwards, with advancing and receding angles. The twin camera arrangement allows for the acquisition of the complete three-dimensional motion of the bat. Low light conditions were preferred because the bats are nocturnal and PIV measurements require a reduced light condition. As the bat flies through the flight cage, it trips a laser beam-break sensor, which initiates the data acquisition sequence.

Wind tunnel

The low speed wind tunnel has a closed-circuit design and has a test section measuring 3.8 meters in length, with a cross-section of 0.60 by 0.82 m (height x width). Although the free-stream turbulence level of the tunnel is quite low (0.29% at 2.81 m/s), a fine-mesh net is placed at the upstream entrance to the test section to restrict the bats, and this results in a turbulence level of 0.5% at 2.8 m/s at the location of the PIV observation area. Antireflective glass plates on bottom, top, and portions of the side of the test section, and Plexiglas windows on the walls allow almost unhindered visibility. The bats are introduced to the flow by a member of the research team at a station approximately 0.5 meter downstream of the measurement section. They flow into the oncoming air stream, moving slowly up the test section towards the settling chamber. Having flown sufficiently upstream and beyond the measurement volume, they are "retrieved" from the test section by a second research team member. The test section is sufficiently long (3.8 meters) such that the measurement area is far from the points of introduction and retrieval, and during measurements, Plexiglass doors were closed to prevent the generation of any additional turbulence in the test section. We define a right-handed

coordinate system with positive x defined in the direction of the wind (negative in the flight direction of the bat). The z -coordinate is positive in the vertical upward direction, and y is positive from center of the bat towards the tip of the right wing. Our results are presented usually in a bat-centered coordinate system, but sometimes in a combination of wind tunnel and bat-centered coordinate systems, with y and z in bat-centered coordinate system (with the origin located between the shoulder blades), but with the origin of the x -axis fixed at the plane where PIV measurements were acquired.

Kinematics

We carried out several kinematic analyses in the course of this project. We describe here general aspects of these methods, followed by those specific to particular experiments.

Kinematic data were recorded by 2 to 4 cameras (Photron 1024 PCI, resolution 1024×1024 pixels, 200 fps) positioned above and alongside the test section or flight chamber. We used the video to reconstruct the positions of markers over time. Where a marker was not visible to at least two cameras, its position could not be calculated, and we filled these gaps in the kinematic data with a custom curve-fitting algorithm based on over-constrained polynomial fitting. For contiguous gaps in the data, with sufficiently rich data at the end points, a third order, over-constrained polynomial fit was used. For gaps that included sporadic intermediate points, a sixth order polynomial was used. After gap-filling, we used a 50 Hz lowpass Butterworth filter to remove high-frequency noise. This cutoff frequency was around 4.5 times higher than the highest wingbeat frequency we recorded (10.4 Hz).

Kinematics of speed change

We employed proper orthogonal decomposition (POD) as a means to summarize and quantify the complexity of wing motions with changes in forward flight speed. For POD of the marker positions, the three-dimensional coordinates of each of the 17 markers through the trial were placed in a matrix. The x , y , and z coordinates of the anterior sternum marker and the y and z values of the posterior sternum marker remained at zero at all times by definition, and were therefore omitted. As a result, the size of the matrix, using 17 markers, was $t \times 46$, where t is the length of the trial, in milliseconds. We subtracted the mean values for each column from all values in that column, and performed POD using singular value decomposition of the transposed matrix in MATLAB (Chatterjee, 2000). For POD of joint angles, we repeated this procedure for the matrix of joint angles.

When the percentage of original motion captured by cumulative POD modes is plotted against the number of modes used, the curve asymptotically approaches 100%, until the motion is completely described when all modes are included. As a summary statistic of that curve for each POD analysis, we used the number of modes required to describe 95% of the movement, $\xi_{95\%}$. To calculate this, we made a spline fit through the aforementioned curve, and defined $\xi_{95\%}$ as the x -axis value where that function crossed 95%; higher $\xi_{95\%}$ values indicate greater dimensional complexity. To determine whether the kinematic complexity of wing motions changed with speed, we carried out linear regressions of $\xi_{95\%}$ versus speed. This was done twice, once for the motion of points and once for the motions of joint angles. Because no two wingbeats were kinematically identical, it is possible that the number of wingbeats could influence the kinematic complexity of a trial. If so, trials with fewer wingbeats would have

lower $\xi_{95\%}$ values than trials with more wingbeats. We looked for this trend in our data, to verify that treating all trials equally, regardless of number of wingbeats, was justified.

We used POD to quantify the relative complexities of motion revealed by varying numbers and positions of wing markers. To assess complexity, we performed POD on every possible combination of markers, from the two sternum markers alone to the complete 17 skeletal markers. This required $2^{15} = 32,768$ separate POD analyses per trial. For each number of markers, we sought the set that captured the highest degree of dimensional complexity. We were unable to use $\xi_{95\%}$ however, since for small numbers of markers, the $\xi_{95\%}$ value is difficult to calculate due to the small number of points through which a spline is to be interpolated. Instead, we used a value we call $P\xi_1$: the percentage of original motion captured by the first POD mode divided by the number of degrees of freedom that went into that POD analysis (e.g. 3 for 1 wing marker, to 45 for 15 wing markers). Sets of markers that move independently of one another should be characterized by a relatively lower $P\xi_1$ value. We used the mean $P\xi_1$ value for each marker set across the nine trials as an index of dimensional complexity for that marker set. We also used POD to quantify the similarity of motion for all 190 pairs of joints ($20 \text{ choose } 2 = 190$). For each pair, POD was performed on the matrix of joint angles, and $P\xi_1$ was calculated. A cluster tree was then constructed using the average linkage function in Matlab, which uses the average distance between all pairs of objects in each cluster, using $(1 - P\xi_1)$ values to form the dissimilarity matrix. The result was a dendrogram of joint angles that clustered joint angles based on similarity of motion

Turning flight

Rotations around the body-centered X_b , Y_b , and Z_b axes were designated roll, pitch and yaw, respectively, following aerodynamic conventions (Phillips, 2004). Body angular velocities were calculated by applying a classical transformation from the angular velocities of the Euler angles, commonly used in rigid body dynamics (Phillips, 2004). Because bats were recorded mid-turn, they already had an initial 'pitch' and 'roll' angles relative to the global coordinate system. These angles were added to the angular velocity cumulative sum and represent the angular body position with respect to the beginning of the recorded portion of the turn. Yaw initial orientation was arbitrary, but because it has no systematic effect on flight control, all trials started with zero degree yaw angle (following Card and Dickinson, 2008). Body angular accelerations were calculated as the first derivative of the body angular velocities over time.

Although the wings of the bat comprise a relatively small fraction of the overall weight of the bat (Thollesson and Norberg, 1991), the motions and accelerations associated with wing flapping may produce substantial inertial effects. As a result of these morphing motions, the CoM of the bat will not correspond to a fixed anatomical location on the bat during flight. To account for the wing displacements in the determination of the location of the center of mass, we constructed a mass model representation of the bat. The mass model is a time varying, discrete mass approximation of the bat mass distribution, based on the location of the markers. To develop the discrete mass system representing the bat, we partitioned total body mass into individual components or regions. The wing membrane, wing bones and trunk were treated as separate masses which were combined to form the total mass model. To model the mass distribution of the membrane, we constructed a triangulation of the wing geometry at each time step. The large-scale, base triangulation was developed using the location of the marker positions at any given time, and a subsequent subdivision of those triangles was performed to give a mesh of fine-scale triangular elements.

Each triangle element (T_i) on the membrane was assigned a constant thickness (1×10^{-4} m) and density (1×10^3 kg m⁻³), based on measured characteristics of bat wing membrane skin (Swartz et al., 1996). A resulting discrete point mass (m_i) for each triangular membrane element was computed based on the volume of that triangular membrane and assigned a position at the centroid of the triangle element. To model the distribution of mass among and within each of the wing bones, we constructed a curve between the markers at the endpoints of the bones. The curve for each bone in the wing was defined from the location of the markers, and the mass of the fourth digit, that we did not track, was divided equally between the third and fifth digit. Given the tapered shape of bat bones (Swartz, 1997), the cross-sectional radius of each bone element of the model was defined by a quadratic function with respect to the length of the bone. We assigned a constant density to the bones (2×10^3 kg m⁻³). Using the distribution of bone radii distribution and the location of the bone elements in space, the line was subdivided into smaller line elements, from which discrete mass points were defined. The mass of the wings was scaled such that the constructed distribution represents the 16% of the total body mass, according to measurements of bats of similar size (Thollesson and Norberg, 1991). The mass and moment of inertia of the wing with respect to the shoulder was compared to measured values (Thollesson and Norberg, 1991) to ensure that the model represents the physical reality. Finally, the bat's body was defined as a three-dimensional ellipsoid divided into discrete mass points. The discrete mass representation of the membranes, bones and body was combined with detailed kinematic records of motion of each landmark to determine the center of mass of each one of the mass elements, m_i , using the equation:

$$\vec{r}_{CoM} = \frac{\sum \vec{r}_i m_i}{m_T}$$

where \vec{r}_{CoM} represents the position vector of the CoM, \vec{r}_i represents the position vector of the i -th discrete point mass and m_T represents the total mass of the bat.

Net body velocity (**Vb**) and acceleration (**Ab**) vectors were calculated as the first and second derivatives of the position vector of the CoM in the global coordinate system. The global trajectory of the bat (i.e., the flight direction) in the horizontal plane was defined as the bearing angle (ϕ) and it was calculated as the angle between the horizontal component of the net body velocity vector (**Vb_{xy}**) and the Xg axis (Fig. 6). Changes in heading can be described as a rate of turning known as curvature (κ). Curvature is defined as the inverse of the radius of the curved path and is calculated by the equation

$$\kappa = \frac{|V_{b,xy} \times A_{b,xy}|}{|A_{b,xy}|}$$

where **V_{b,xy}** and **A_{b,xy}** are the velocity and acceleration of the body in the horizontal plane Xg–Yg, respectively.

Differences in the angle of attack of the two wings during a wingbeat cycle could have aerodynamic influence that results in turning. Angle of attack was calculated for each wing as the angle between the relative incident air velocity of the wrist marker (*wst*) and the plane of the hand wing, defined by the markers on the wrist (*wst*), fifth digit (*d5*) and the wingtip (*d3*). The exact calculation of angle attack requires the estimation of the induced velocity on the wing

(i.e., wake and wing-bound vortex velocities) (Aldridge, 1986b) but we ignored induced velocity, because our analyses focus on comparisons between left and right wings, and induced velocities are similar for the two wings. The difference in the surface area between left and right wing was estimated by calculating the wrist angle, a measure of the flexion/extension of the wing as a proxy. Wrist angle was defined as the interior angle of the triangle formed by the chest (*ch*), wrist (*wst*) and wingtip (*d3*) markers for each wing. Thus, when wrist angle is large, wing surface area is also large.

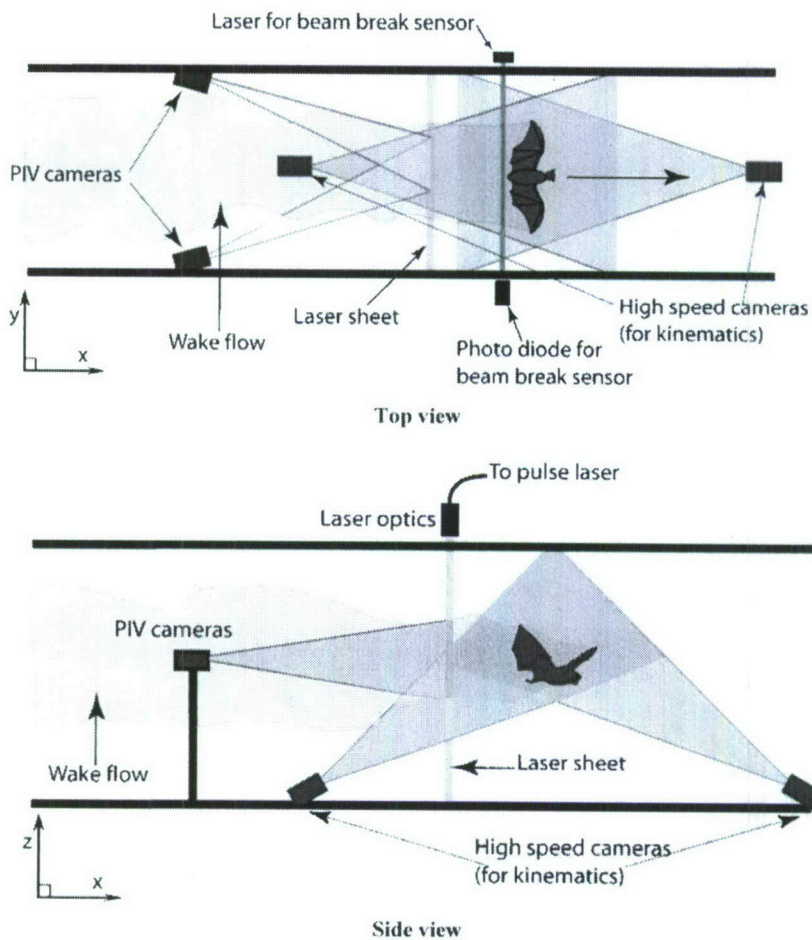
Downstroke and upstroke phases of the wingbeat were defined by positive and negative velocities of the wrist in the Z_b direction, respectively. The vertical (γ_v) and horizontal (γ_h) stroke plane angles were defined as the major axis of the projection of the wingtip with respect to the body on the X_b-Z_b and X_b-Y_b planes, respectively. These major axes were estimated by fitting a least-square line for each wingbeat.

Changes in body rotations could be potentially explained by differences in profile drag produced between the two wings. A possible mechanism to modulate drag is to alter the wing area exposed to the airflow. Lateral projection of the wing can be used as a proxy for wing area exposed, where wings that are more extended should present larger wing areas. We estimated the lateral projection as the distance of the wingtip marker to the midline of the body in the global coordinate system.

To avoid the problem of autocorrelation and pseudoreplication among wingbeats, kinematic parameters were calculated from one representative wingbeat per trial. We defined the representative wingbeat as the one with a heading angle the closest to 45 degree from the initial orientation of the flight. This wingbeat represented a mid-turn wingbeat and usually presented the maximum rate of change in heading angle and in body angular velocities. In some cases, these variables peaked ± 1 wingbeat from the wingbeat defined by the heading angle criterion and the former was used. For most of the analyses, a sample size of 32 trials was used and values are reported as mean \pm s.e.m. unless specifically indicated. Statistical analyses were conducted using JMP 6 (SAS Institute, Cary, NC, USA) and MATLAB R2006a (The Mathworks, Inc., Natick, MA, USA). Regression analyses were performed with general linear models (GLM) to control for differences among individuals

PIV

In the flight cage, after a pre-set delay, typically 300 ms, calculated to allow the bat to pass through the measurement volume, the wake flow is illuminated by a sequence of laser pulses using a pair of Nd:YAG lasers (5 ns, 150 mJ/pulse, typically 1000 μ s between adjacent images, 200 ms between adjacent image pairs). The laser beam is guided through a series of beam-



Schematic of the experimental setup for the measurement in the transverse (Treffz) plane. The bat flies from left to right and triggers the acquisition sequence by triggering a beam-break sensor. The wake is imaged in a plane behind the animal, after she has passed through.

forming optics, which spread out in a thin laser sheet from the flight cage ceiling. The test section is seeded with a light mist of micron-sized aerosol particles of DEHS (di-ethylhexyl-sebacate) generated by a custom-built Laskin nozzle fog generator. This fine mist is non-toxic and appears to have no effect on bat behavior. The motion of the tracer particles is captured by a pair of high-resolution CCD cameras (LaVision FlowMaster3 system, image size: 1376 × 1040 pixels). Both PIV cameras are mounted on a frame and their heights are adjusted at the level of the bat's flight. The velocity field is extracted using standard 3D stereo PIV procedures from the pair of images (LaVision PIV software). By piecing together several image pairs captured from the wake as a function of time, a complete portrait of the wake flow behind the animal can be acquired.

To obtain the wake velocity components in the wind tunnel, we performed time-resolved PIV using a 200Hz double-pulse Nd:YAG laser (Litron LPY 703-200) to illuminate the observation area (pulse duration 6ns, energy 60mJ). The wind tunnel is seeded with di-ethyl-hexyl-sebacate (DEHS) using a custom built Laskin-type nozzle fog generator.

Two high-resolution CMOS cameras (Photron 1024 PCI, resolution 1024×1024 pixels) capture the motion of the DEHS particles in the observation area. The two PIV cameras were located at the downstream end of the test section, and positioned perpendicular to the flow stream so as to capture the wake structure in the Trefftz (y - z) plane. The two cameras imaged overlapping but separate fields of view to maximize the size of the observation area. A single calibration plate and the coordinate system origin were visible in both cameras, and the overlap was approximately 0.05 m, and the resulting image size was 0.23 m x 0.41 m. This field of view was sufficient to image the complete wake of the left wing; in our analyses, we mirrored this wake structure to visualize the entire wake for ease of viewing, using the assumption that left and right wing motions differ little in straight, steady flight.

We recorded PIV data using a buffer loop function to record the data in an endless loop triggered by an END signal (DaVis 7.13 software, LaVision). The calibration parameters are achieved by using the pinhole calibration, and the two camera images stitched together within the software. Vector fields were calculated using cross-correlation with multi-pass iterations with decreasing size (128x128, 2 iterations to 64x64, 2 iterations, 50% overlap). Vectors with peak ratio $Q < 1.2$ and variations to the average neighborhood $> 1.5 * \text{r.m.s.}$ of neighbor vectors were replaced via interpolation in the post processing process and a simple 3x3 smoothing filter was applied. The vector field was exported and subsequently processed in Matlab®.

Circulation (Γ) was obtained by integration of the vorticity (ω_x) over the area to the right of the body marker. The circulation was normalized by the true flight velocity, combining the wind speed (U_∞) and the bat speed (U_B), and the average wing chord ($\gamma = \Gamma / (U_\infty - U_B)c$). We calculated local circulation maxima and minima and defined the wing beat cycle as the period between two minima. The flapping frequency (f_P) was calculated according to the period. However, due to the movement of the bat in the test section, the wake frequency can be different from the true flapping frequency due to a Doppler shift:

$$f_c = \frac{(U_\infty - U_B)}{U_\infty} f_P$$

where f_c is the flapping frequency, f_P is the frequency measured by the PIV in the wake. U_∞ and U_B are the free stream velocity and velocity of the bat (relative to the wind tunnel test section, positive downstream) respectively. We have also assumed that the wake vortex travels at the free stream velocity. The actual flapping frequency was also extracted directly from the kinematics (f_K) and compared with the observed flapping frequency (f_P) and calculated flapping frequency (f_c). Small variations in the flapping frequency of consecutive wing beat cycles led to a variable number of computed values of the velocity field and circulation during each cycle (approximately 28-31), and to address this, we partitioned each wing beat cycle into thirty-five segments and used interpolation to compute the circulation for thirty-five time increments per wing beat cycle. We estimated a moving average over three values, and then computed mean circulation over six wing beat cycles. To visualize the development of wake structure over time, we reconstructed vorticity isosurfaces from PIV measurements in the Trefftz (y - z , or transverse) plane, converting time to streamwise distance by assuming, as before, that the wake structures advect with the freestream velocity. The surfaces are plotted using a 3x3 smoothing filter and vorticity threshold ($\pm 15 \text{ s}^{-1}$) which allows the main vortex structure to be visualized.

Kinematics with PIV

The cameras were synchronized with the PIV recordings by using the laser flash lamp sync signal to trigger a digital delay-pulse generator (Model 555 Berkeley Nucleonics Corporation). Kinematic and PIV cameras shared a single origin and coordinate system; calibration was achieved with the direct linear transformation (DLT) method (Abdel-Aziz and Karara 1971) following videographic recording of a calibration plate mounted on a linear traverse, moved through the control volume by successive displacements of 0.1 m. 17 white dots marked the joints and important anatomical positions on the dorsal surface of the bat (Figure 3). Gaps in the data due to obstruction of the markers were filled by interpolation. The kinematic measurements were sub-sampled by a factor of ten using a spline interpolation. This proved convenient to ensure the accuracy of the correlation between the PIV and kinematic measurements, as well as during the correction of the PIV data to account for the Doppler shift described above.

Light

To minimize light pollution, the PIV cameras were equipped with 532 nm band-pass filters transmitting light mostly in the range of 511-548 nm. Narrower filters darkened videographic images significantly and were not usable. The kinematics volume was illuminated by three Xenon strobe lights (Nova-Strobe dax, Monarch instrument) operating at 200 Hz, and synchronized with the kinematics cameras. The strobe lights emit short (10-25 μ s) intense light pulses which provides sufficient illumination for the kinematic recordings, eliminates motion-induced blurring while maintaining a low average light level (which is preferred by the nocturnal bats). By pointing the strobes away from the PIV cameras, we kept reflections to a minimum. This approach also allow for the possibility of interlacing the PIV lasers with the strobe lights, thus further reducing PIV light pollution. However, this was not found to be necessary and was not used in the current experiments.

Light curtain

The intense energy in the PIV laser light sheet is capable of injuring the bats (particularly their eyes), and so the operation of the PIV system was gated by a laser light safety curtain, positioned 0.05m upstream of the laser light sheet, and consisting of an array of 21 low power red diode lasers spanning the entire test section, each aimed at a complementary photo-diode. After the bat was released and had safely advanced upstream of the light curtain, the system was activated. If the bat moved downstream stream for any reason, it would interrupt one of the safety beams, at which point the laser system was automatically shut down.

PRIMARY RESULTS

Kinematics

Straight Flight

Wingbeat kinematics

Flight speeds of *C. brachyotis* in the wind tunnel ranged from 3.2 to 7.4 m·s⁻¹. Wingbeat

frequencies (9.4 ± 0.6 Hz, mean \pm S.D.) were similar to those reported previously for other bat species flying in still air (Norberg, 1976a), and increased slightly with increased flight speed (frequency = $0.33 \times \text{speed} + 7.8$; $F = 15.9$; $n = 9$; $r^2 = 0.69$; $P = 0.0053$). In slow flight, the downstroke brought the wing anteriorly and ventrally (forward and down), and the upstroke moved it posteriorly and dorsally (backwards and up). Low speed flight kinematics also included a wingtip reversal on the upstroke, whereby the wingtip moved backwards relative to the air around it. At higher speeds, the fore-aft component of that motion was diminished, so the wings moved mostly dorsoventrally (up and down), and without wingtip reversal. These kinematic descriptions resemble those reported for other bats in previous studies (Aldridge, 1986).

Proper Orthogonal Decomposition

Each mode resulting from Proper Orthogonal Decomposition of marker positions describes a range of motion of the markers in 3-dimensional space. A convenient way to visualize the range of motion captured by any given mode is to project the original motion of the markers onto the subspace defined by that mode (e.g. Bozkurttas *et al.*, 2006). When a linear coordinate system is used, the positions of each marker in a POD mode lie on a straight line. In this study, projection of the wing kinematics onto the first mode of POD resulted in a simple flapping motion of the wings. For slow flights, the wings moved up and down with a fore-aft component relative to the body axis, and in faster flights the motion contained less fore-aft motion, and was restricted to up-down movement. These trends mirror the decrease in the fore-aft component of wing flapping with increasing speed that we observed from the kinematics. From POD of marker positions, the first mode described $31.4 \pm 2.8\%$ ($n = 9$) of kinematic movement, and the amount of variation explained by subsequent modes decreased rapidly. For any trial, 7 modes were required to explain $>80\%$ of the motion, 11 modes were needed to explain $>90\%$ of the motion, and 16 of the total 46 orthogonal modes were needed to explain $>95\%$ of the motion. The mean $\xi_{95\%}$ value for the 9 trials was 13.5 ± 1.2 . Using joint angles instead of marker positions, $22.4 \pm 1.8\%$ of motion was explained by the first mode, and the mean $\xi_{95\%}$ value was 13.1 ± 0.8 (Figure 3b). We found no influence of the number of wingbeats included on P_{ξ_1} (linear regression $P = 0.89$). However, $\xi_{95\%}$ values did increase slightly with the number of wingbeats in a trial ($\xi_{95\%} = 1.57 \times \text{number of wingbeats} + 8.60$; $r^2 = 0.58$; $P = 0.02$). Depending on whether one uses P_{ξ_1} or $\xi_{95\%}$ to measure complexity, the number of wingbeats in each trial may or may not need to be equal in all trials for them to be compared. To equilibrate the number of wingbeats for all trials, while losing the least possible information, one could discard a wingbeat from both of the four-wingbeat trials, and the two-wingbeat trial altogether. When we employed this procedure, the regressions of P_{ξ_1} and $\xi_{95\%}$ with speed showed the same statistical trends obtained with the complete data set (reported below). We therefore elected to treat all trials equally in our analyses, and did not weight them based on the number of wingbeats.

Changes in dimensional complexity with speed

Dimensional complexity varied little between trials, and did not change significantly with speed. For the marker position data, flight speed had no significant impact on $\xi_{95\%}$ values ($\xi_{95\%} = -0.16 \times \text{speed} + 14.28$; $r^2 = 0.04$; $P = 0.61$). Using joint angle data, $\xi_{95\%}$ values

increased slightly with increasing speed ($\xi_{95\%} = 0.30 \times \text{speed} + 11.62$; $r^2 = 0.32$), but not significantly so ($P = 0.11$).

Testing the efficacies of kinematic marker positions

For each of the 32,767 possible combinations of 1 to 15 wing markers (3 to 17 body markers), we calculated $P_{\xi 1}$ for all nine trials, and used the mean $P_{\xi 1}$ value for each marker combination for analyses ($n = 9$ trials; Figure 4). As expected, using more markers generally resulted in higher dimensional complexity overall (lower $P_{\xi 1}$ values), and for a given number of wing markers, the positions of those markers influenced the capture of actual dimensional complexity. Markers at the shoulder and hip contributed substantially to the dimensional complexity of kinematics. One possible explanation for this pattern is that more muscle is interposed between the skin and underlying skeleton at the shoulder and hip compared to other anatomical markers, potentially leading to increased skin motion artifact. Our analysis demonstrates that the knee moves independently relative to forelimb markers, and that the 5th digit contributes relatively little motion that is independent of other parts of the wing. These trends are revealed by the consistent appearance of those anatomical markers in the sets of lowest $P_{\xi 1}$ values for a given number of markers. We observe these trends whether the shoulder and hip are included or excluded during analysis.

Assignment of joint angle groups

Correlations of motion (mean $P_{\xi 1}$ values) among the 190 joint angle pairs varied, with a left-skewed distribution (min 51.1%, max 83.2%, median 59.3%). Using a similarity threshold of 0.7, we found three groups of joint angles based on the cluster analysis. The first group (joint angles 3, 6, 7, 11, and 12) includes the angles between digit V and its neighbouring long bones (the forearm and digit IV), along with the metacarpophalangeal angles of digits III and IV, and rotation of the humerus. The second group (joint angles 4, 8, 9, and 10) includes the carpometacarpal angle of digits III, IV, and V, along with the elbow angle. The third group (joint angles 1, 2, 17, 19, and 20) includes the elevation/depression (dorsoventral) and protraction/retraction (craniocaudal) of the humerus, the elevation/depression of the femur, femoral rotation, and the knee angle.

Straight Flight Kinematics Summary:

By delineating the wing kinematics of a flying bat in terms of quantitative dimensional complexity, we processed complex motion to uncover three functional groups of joint angles that should be useful in a broad variety of contexts, including morphology, aerodynamics, and neurobiology. Each group consists of joint angles that move in highly correlated ways during steady flight, and provides a starting point to discern functional units of aeromechanic or neuromuscular relevance for bat flight. Where accurate kinematic reconstruction is the goal, our results demonstrate that in addition to the commonly used kinematic markers on the wing, the hindlimb should be tracked, and that several parts of digits III and IV must be tracked independently. Also, we found that the bat changed the complexity of motion only slightly with changes in speed, even though the motions of the wings changed in a way that resulted in different flight speeds.

Turning Flight

General description of the turn

When turning, bats flew consistently at low forward speeds of $2.0 \pm 0.1 \text{ m s}^{-1}$ ($N=53$) and maintained relatively constant speed in the X_z direction throughout the calibrated volume, though for some trials, flight speed decreased at the end of the sequence. In a typical turn, bats gained altitude during the first half of the turn ($0.12 \pm 0.04 \text{ m}$, $N=53$) and then maintained their height after turning, thereby increasing their net altitude during the turn. Changes in bearing occurred almost entirely during the downstroke, with an average change of 16.0 ± 0.8 degrees per wingbeat. We captured, depending on the flight speed, between 2 and 4 wingbeats within the calibrated space. Extrapolating the mean change in heading during a wingbeat cycle to the whole turn, *C. brachyotis* would complete a 90-degree turn in about 6-7 wingbeats. This is likely to be an overestimation, as the change in heading tends to peak towards the middle of the turn. From a preliminary study of *C. brachyotis* performing the same task, a 90-degree turn was completed in about 6-9 wingbeats (J. Iriarte-Diaz, unpublished). Bats reached maximum changes in bearing of 416.9 ± 26.4 degrees s^{-1} near mid-downstroke, producing turns with a minimum turning radius of $0.290 \pm 0.031 \text{ m}$ (curvature of $5.53 \pm 0.62 \text{ m}^{-1}$), about 0.8 wingspans. Mean curvature during downstroke was $3.36 \pm 0.33 \text{ m}^{-1}$.

Changes in body orientation

Bats consistently changed their body orientation throughout the wingbeat cycle in a sinusoidal fashion with a frequency equal to the wingbeat frequency (Fig. 8). Bats rolled into a bank at the beginning of the turn. Average bank angle over a wing stroke was 25.8 ± 2.0 degrees with a maximum of 56.3 degrees. Bank angle reached a maximum at mid-downstroke and a minimum at mid-upstroke with an absolute change of 10.6 ± 1.1 degrees per half-stroke. Despite the apparent variation within a wingstroke, average bank angle did not change among wingbeats within each trial (paired *t*-test, $t_{31}=0.84$, $P>0.1$; Fig. 9A). Similarly, elevation angle showed changes within the wingbeat cycle, with an average difference of 10.6 ± 1.1 degrees per half-stroke, reaching a maximum at mid-downstroke and a minimum at mid-upstroke, but with no significant changes between wingbeats (paired *t*-test, $t_{31}=-1.55$, $P>0.1$). Mean elevation angle was 25.7 ± 2.5 degrees. Heading angle, however, showed a significant between-wingbeat component (paired *t*-test, $t_{31}=13.58$, $P<0.0001$), as expected in a turn, as bats have to continuously change their body orientation to keep it aligned with their bearing. During upstroke, bats increased their heading angle an average of 20.8 ± 1.9 degrees, rotating towards the direction of the turn. Angular velocity and angular acceleration profiles were very similar for all three angles. During upstroke, angular velocities increased reaching a peak around the upstroke-downstroke transition of 363.5 ± 23.7 , 217.2 ± 20.5 and 104.3 ± 23.3 degrees s^{-1} for heading, elevation and bank angles, respectively. Angular accelerations showed a clear pattern of positive acceleration for all three angles throughout upstroke and a very strong negative acceleration around the middle of the downstroke.

Changes in body angles

Pitch angle showed high within-wingbeat variation, reaching a minimum at mid-upstroke and a maximum at mid-downstroke, with an average change of 12.1 ± 0.9 degrees per half-stroke. Yaw angle increased constantly throughout the wingbeat, and showed a difference of 13.7 ± 1.0 degrees between the end and the beginning of the wingbeat (paired *t*-test, $t_{31}=12.4$, $P<0.0001$) that resulted from positive yaw angular velocities throughout the

wingbeat (Fig. 9E). In contrast, roll angle decreased over the wingbeat, decreasing during the upstroke and remaining constant during downstroke. Over a wingbeat cycle, roll angle decreased -4.3 ± 1.1 degrees (paired *t*-test, $t_{31} = -4.0$, $P < 0.0001$). Yaw angular velocity was positive throughout the wingbeat, in contrast to roll angular velocity, which was mostly negative.

Pattern of change in heading and flight direction

Heading and bearing angle varied in a similar fashion throughout the wingbeat cycle, with changes of similar magnitude, but with a clear offset between them. Heading angular velocity peaked at the upstroke-downstroke transition, although bats changed bearing the most at the middle of the downstroke, indicating that changes in heading preceded changes in flight path during the turn. The difference between heading and bearing angle peaked at the upstroke-downstroke transition, and reached a minimum at the end of the downstroke.

Wingbeat kinematic parameters

Bats flew using wingbeat frequencies of 9.2 ± 0.1 Hz, with upstrokes comprising $56 \pm 2\%$ of the stroke cycle. Wingtip speed with respect to the body showed a sinusoidal variation with a frequency of nearly half of wingbeat frequency (Fig. 11A). Wingtip speed reached a minimum of 4 m s^{-1} at mid-upstroke and a maximum of about 8 m s^{-1} near the end of upstroke and at mid-downstroke (Fig. 11A). Wrist velocity showed less variation during the stroke cycle, with a mean speed near 3 m s^{-1} (Fig. 11B). Mean downstroke speed was 6.31 ± 0.11 and $2.97 \pm 0.10 \text{ m s}^{-1}$, for the wingtip and wrist, respectively. During a half-stroke, angle of attack changed from around 50 degrees at the beginning of downstroke to about 20 degrees at the end of downstroke, with a mean of 26.7 ± 0.7 degrees. Vertical stroke plane angle, γ_v , was 52.7 ± 4.8 degrees. Wing kinematics in the body coordinate system were very similar for the inside and outside wings, although small but statistically significant asymmetries were observed. Mean wingtip speed of the inside wing was 7% faster (a difference of $0.27 \pm 0.15 \text{ m s}^{-1}$; paired *t*-test, $t_{31} = 1.82$, $P = 0.08$), particularly during the upstroke. No significant differences in speed between the two wings were observed at the wrist. These differences are mostly due to higher wingtip lateral velocities of the inside wing during the beginning and the end of the upstroke. The angle of attack of the inside wing during downstroke was 9% larger (a difference of 2.7 ± 0.9 degrees, paired *t*-test, $t_{31} = 3.15$, $P < 0.01$) than the outside wing. Also, the wrist angle, a measure of the extension of the hand, and likely of the surface area of the wing, was larger in the inside wing by 3.3 ± 0.7 degrees (paired *t*-test, $t_{31} = 4.18$, $P < 0.001$). Even though elbow angle was not measured, we believe that this angle reflects overall wing extension, as we also found no major differences in the distance of the wingtip to the midline of the body throughout the wingbeat. The largest kinematic difference was found in the horizontal stroke plane angle γ_h . The asymmetry in γ_h during turning was 10.8 ± 2.8 degrees (paired *t*-test, $t_{31} = 3.86$, $P < 0.001$), indicating that the outside wing moved more parallel to the body than the inside wing, which had an overall direction more oriented towards the midline.

Kinematic correlations with changes of direction

In a roll-based maneuver, the centripetal force that produces the turn depends on the roll angle. The greater the roll, greater the centripetal force and tighter the turn. In such a case, the rate of change in direction angle is expected to be proportional to the roll angle (McCay, 2001). On the other hand, in a yaw-based maneuver, the change in direction should be related to the rate of change in yaw rather than yaw orientation (Warrick et al., 1998; Hedrick and Biewener, 2007). Both heading angular velocity and mean bank angle during

the downstroke are significantly correlated with the peak rate of change in direction (GLM, $r^2_{adj}=0.88$, $F_{4,44}=92.7$, $P<0.0001$ and GLM, $r^2_{adj}=0.72$, $F_{4,44}=32.48$, $P<0.0001$, respectively). In a multiple regression model, controlling for individual effects, only heading angular velocity was significant (GLM, $r^2_{adj}=0.89$ for the whole model; heading angular velocity effect: $\beta=0.82$, $F_{1,43}=63.5$, $P<0.0001$; bank angle effect: $\beta=0.13$, $F_{1,43}=1.6$, $P>0.2$). The partial correlation between heading rate and bearing rate while controlling for bank angle was $r_{heading|bank}=0.80$ (two-tailed t -test, $P<0.0001$), while the partial correlation between bank angle and bearing rate when controlling for heading angular velocity was $r_{bank|heading}=0.14$ (two-tailed t -test, $P>0.05$). Based on the instantaneous acceleration of the CoM estimated from the mass model (see Methods, above), it is possible to calculate the total instantaneous centripetal acceleration ($A_{c,total}$) necessary to produce a turn with a radius $1/\kappa$ using:

$$A_{c,total} = (V_{b,xy})^2 \kappa$$

where $V_{b,xy}$ is the forward speed of the estimated CoM in the horizontal plane of the lab X_g - Y_g , and κ is the curvature of the turn. Given the symmetry in the wing kinematics in the body coordinate system, we can estimate the centripetal component produced by the banked orientation of the body, by assuming that the net aerodynamic force is oriented perpendicular to the bank angle. Thus, the bank component of the centripetal acceleration was estimated as

$$A_{c,bank} = (A_{CoM,z} + g)_z = \tan\phi \cos(\psi - \phi)$$

where $A_{CoM,z}$ corresponds to the vertical acceleration calculated from the position of the CoM, and g corresponds to the acceleration of gravity. On average, $A_{c,roll}/A_{c,total}$, the estimated centripetal acceleration produced by the degree of bank relative to the centripetal acceleration necessary to produce the observed change in flight direction, accounted for only $74.0 \pm 4.9\%$ of the total acceleration required. In some cases, the bank contribution was as small as 10% of the necessary centripetal acceleration, but in a few others, bank angle accounted for almost all of the acceleration needed to produce the turn.

Turning kinematics Summary:

Bats carried out low speed 90-degree turns by primarily using a crabbed mechanism to redirect their net aerodynamic force and thus produce centripetal force towards the direction of the turn. We found that turns can be divided into two functionally different components associated with the portions of the wingstroke cycle. In the first part of the turn, during upstroke, bats rotated their bodies horizontally into the turn without significant changes in flight direction. As a result, at the onset of downstroke, the body was already oriented toward the direction of the turn, so that forward component of the net aerodynamic force was also oriented towards the center of the turn. In the second part, which occurred during downstroke, bats changed their flight direction. The centripetal force necessary to change the heading of the CoM, however, was produced by a combination of the forward and the dorsal component of the net aerodynamic force. The dorsal component, which is parallel to the mid-sagittal plane of the bat's body, arose from the banked attitude of the body through which the vertical component of the net

aerodynamic force was reoriented toward the center of the turn. The forward component was modulated by the heading rotation of the body that occurred during the first part of the turn. The analyses presented here do not support our prediction that bats use a banked turning mechanism, like those described for other flying organisms. However, they also indicate that turning in bats is aerodynamically and kinematically complex, and includes a distinctive use of the upstroke phase, usually ignored in studies of animal flight.

PIV

PIV data analysis

PIV images were taken at both the transverse (*Treffz*) and streamwise (*Parasagittal*) planes. Because of the limitations of the PIV system (lowsampling rate, limited image view) and the complexity of the bat's flight, PIV data in the streamwise plane will be further investigated at some later time. Discussions here will only focus on the transverse plane where the largescale vortex structures were most clearly visible. The view of PIV images were 26.5 cm²—20 cm with a total of 82°—62 vectors extracted. It is evident that there is a strong wing tip vortex generated by the bat's flight. The vortex decays in strength, and advects downwards. Since the vortex is well defined, the vorticity, ω , can be determined based on Stokes' theorem from calculation of the circulation, Γ , via contour integration normalized by the area enclosed by the contour composed of differential elements dr (Batchelor 1967):

$$\iint_A \omega \cdot dA = \oint u \cdot dr$$

The integration is performed along the edges of 1X 1 square interrogation windows using the velocity values at the square's vertices. This vorticity calculation is performed with no oversampling of the interrogation windows and generally provides a more accurate estimate of vorticity than is achieved by differentiation of the velocity field (Raffel *et al* 1998). The majority of the flow fields measured in this series of experiments exhibit a complexity which makes the task of defining the vortex core difficult. Within the main core itself, there exist smaller vortical structures. Therefore, one cannot simply define the vortex cores as connected regions of vorticity of the same sign. Thus, an alternative method of defining the vortex core was devised to accommodate these nuanced structures so that the circulation could be estimated from these data.

The circulation was only calculated for several trials where it was visually apparent that a vortex was located in the measurement plane. The circulation of a region can be calculated by integration of the velocity along the contour that is the boundary of this region. For simplicity, this analysis employed circular contours in the circulation calculations. To find the 'center' of the vortex core, a rectangular region was manually selected via visual inspection, with care taken to enclose the majority of the main flow structure. The centroid of vorticity within this rectangular interrogation window was then calculated and was defined as the 'center' of the vortex core. This location served as the point about which a series of integrations about concentric circular contours of increasing radii were performed to determine the magnitude of the circulation as a function of area enclosed. Utilizing the condition that the flow outside the vortex core is irrotational, the vortex core was defined to be the region within which the

circulation reaches a maximum. Although the flight is clearly unsteady, we can use the Kutta-Joukowski theorem for steady flight as a crude estimate of the lift per unit span (Anderson 1984):

$$L = \rho U \Gamma$$

where L is lift per unit span and ρ is air density. Based on the maximum circulation calculated here ($\Gamma/Ub = 0.24$, $b = 0.2$ m, $U = 2.7$ m s⁻¹, $\rho = 1.2$ kg m⁻³), the total lift can be approximately estimated as 0.17 N, which, at the measured flight speed, should be able to support a mass of 17 g. This is comparable to, but underestimates, the measured mass (~40 g), but is, at least, in the right neighborhood, considering the simplicity of this argument and the fact that unsteady effects have not been considered. Clearly, more detailed measures of the circulation and its relationship to the true momentum balance need to be performed, although this is not possible with the slow rate of velocity field acquisition (5 Hz, or approximately every two wing beats) that was available to us for this initial set of experiments.

Each PIV acquisition sequence is, however, accompanied by the complete kinematic history of the flight. This enables features identified in the wake structure to be associated with specific wing/body motions. It is, however, a challenge to couple the PIV and 3D kinematic data because runs differ in flight speed and trajectory. To achieve meaningful data synthesis, we first adjust the coordinate origin and normalize velocity. The velocity field is then non-dimensionalized by the flight speed associated with each particular acquisition. Each run is then rearranged and collated based on the wing beat phase angle. In this manner, we are able to determine the location of the vortex core relative to the bat as well as the relative wing location with respect to the wing beat cycle as it moves through the PIV plane. Accordingly, we can reconstruct a 'cartoon' of the wake shed by the bat as it moves through its wing beat. Our first attempt at this reconstruction is shown in figure 12, although it should be emphasized that this is hindered by the rather small set of realizations available in the ensemble. The main wing tip vortex structures deposited by the bat on the downstroke closely follow the wing tip trace as one might expect. But, in the case of the upstroke, the vortices shed appear to fall outside the wing tip trace. On the upstroke, the animal folds its wings in toward the body to the point where the wing tips may no longer be the outermost extension of the bat. Therefore, the wake pattern suggests that these upstroke vortices are most likely shed from another location along the folded wing, possibly the wrist joint. With this relatively small and preliminary data set, it is too early to be able to say how this cartoon compares with wake vortex structures proposed for the case of bird flight (Rayner 1979, 1987, Spedding *et al* 2003), and more detailed studies are clearly required.

PIV Result Summary

We have performed experiments to capture the coupled kinematics and wake velocities of bats. The kinematics reveals that, at the relatively low flight speeds considered here, bats possess unique flight characteristics, distinct from those observed in both insect and bird flight, including a flexion of the wing during the upstroke compared to the largely extended sweep that characterizes the middle portion of the downstroke. We have also characterized maneuvering flight, in particular a 180° turn, which the bat executes rapidly over a short distance and narrow radius, exhibiting turn rates exceeding 200° s⁻¹. The kinematic data also show that the flight speed and elevation are not constant, but are closely synchronized with wing horizontal and vertical motions. We have successfully employed PIV data to reconstruct

wake geometry which indicates strong wing tip vortices and a complex vortical wake structure, although these need to be verified and explored further. The experiments presented in this paper represent the first detailed measurements to couple wing kinematics and wake velocities of bats, and further research will increase both data quantity and quality. As available instrumentation improves, new experiments will yield more insights into the abilities and underlying biomechanics that these animals exhibit.